Jurnal Elektronika dan Telekomunikasi (JET), Vol. 25, No. 1, August 2025, pp. 55-63
Accredited by RISTEKDIKTI, Decree No: **158/E/KPT/2021**
doi: 10.55981/jet.705

Cardiac Imaging with Electrical Impedance Tomography (EIT) using Multilayer Perceptron Network

Amelia Putri Ristyawardani[a], Marlin Ramadhan Baidillah[b,*], Yudi Adityawarman[b], Pratondo Busono[c], Adityo Rachmadi[b], Meta Yantidewi[a], Endah Rahmawati[a]

[a]Department of Physics
State University of Surabaya
Jalan Ketintang
Surabaya, Indonesia
[b]Research Center for Electronics
National Research and Innovation Agency
KST Samaun Samadikun
Bandung, Indonesia
[c]Research Center for Smart Mechatronics
National Research and Innovation Agency
KST Samaun Samadikun
Bandung, Indonesia

Abstract

This research explores the enhancement of Electrical Impedance Tomography (EIT) for cardiac imaging using Multilayer Perceptron (MLP) networks, focusing on supervised and semi-supervised learning approaches. Using synthetic thoracic datasets simulating dynamic cardiac and respiratory conditions, the study demonstrates that supervised learning achieves lower mean squared error (MSE) values (minimum 4.76) and more stable predictions compared to semi-supervised learning (minimum MSE 5.08). However, semi-supervised learning excels in edge accuracy and noise reduction, particularly in regions with sharp conductivity gradients, making it a viable method for scenarios where labeled data is limited. Dropout regularization at 0.3 provided an optimal balance, enhancing model generalization and robustness. While supervised learning outperformed semi-supervised methods in overall accuracy, the latter showed potential for cost-effective and scalable applications in EIT-based cardiac imaging. These findings suggest that integrating advanced machine learning with EIT can improve diagnostic accuracy and enable efficient use of sparse labeled data, paving the way for future optimizations and clinical applications.

Keywords: Electrical Impedance Tomography, Multilayer Perceptron, Semi-Supervised Learning, Cardiac Imaging, Machine Learning.

I. Introduction

Electrical Impedance Tomography (EIT) has emerged as a vital tool in cardiac imaging due to its non-invasive nature and ability to provide real-time information about the electrical activity and conductivity of cardiac tissues. Traditional imaging modalities such as Magnetic Resonance Imaging (MRI) and Computed Tomography (CT) often involve exposure to radiation and can be costly, making EIT an attractive alternative for continuous monitoring of cardiac conditions[1], [2]. EIT's capability to visualize changes in electrical impedance allows for the assessment of various cardiac functions, which are crucial for diagnosing and managing cardiovascular diseases [3], [4]. By utilizing surface electrodes to measure the electrical conductivity of tissues, EIT provides real-time insights into physiological changes within the thoracic cavity, making it invaluable for assessing both lung and cardiac functions [5], [6]. The integration of machine learning techniques, such as Multilayer Perceptron Networks (MLP), into EIT can enhance image reconstruction and interpretation, potentially leading to improved diagnostic accuracy and patient outcomes [7], [8].

The reconstruction of images in EIT is characterized by its inherent ill-posed nature, where the relationship between the measured boundary voltages and the internal conductivity distribution is complex and non-linear. EIT requires solving complex nonlinear equations to derive internal conductivity distributions from surface measurements, which can lead to artifacts and inaccuracies in the reconstructed images [9]. Traditional reconstruction methods often struggle with these complexities, necessitating advanced techniques to improve image quality and reliability. As a result, machine learning approaches, particularly those utilizing multilayer perceptron networks, have gained traction in enhancing the reconstruction process by learning from large datasets to improve accuracy and robustness [9], [10]. These networks can learn to approximate the nonlinear relationships inherent in EIT data, thereby enhancing the accuracy of the

* Corresponding Author.
Email: marlin.ramadhan.baidillah@brin.go.id
Received: November 29, 2024 ; Revised: February 4, 2025
Accepted: April 25, 2025 ; Published: August 31, 2025

reconstruction process and enabling the extraction of more meaningful features from the imaging data [11].

In the context of cardiac imaging using EIT, semi-supervised learning approaches are particularly advantageous. The medical imaging field often suffers from a scarcity of labeled data due to the time-consuming nature of expert annotations. Semi-supervised learning allows for the effective utilization of both labeled and unlabeled data, thereby improving model performance even when labeled examples are limited [12], [13]. Semi-supervised learning can enhance the model's ability to generalize from a small set of annotated examples while utilizing the vast amounts of unlabeled data that can be collected during routine EIT monitoring [14]. This approach not only improves the performance of the reconstruction algorithms but also reduces the need for extensive manual labeling, which can be time-consuming and resource-intensive in clinical settings [15].

Several studies have explored the application of EIT in cardiac imaging. For instance, Zhang et al. demonstrated the use of deep feature-domain matching to separate cardiac-related components from EIT image series, showcasing the potential of advanced machine learning techniques in enhancing EIT imaging [16]. However, these studies primarily focus on specific algorithms without a comprehensive exploration of MLP or semi-supervised learning approaches, which could further improve the robustness and accuracy of cardiac imaging. Moreover, the literature indicates a growing interest in integrating machine learning techniques with EIT. Rymarczyk et al. discussed the application of various machine learning algorithms for image reconstruction in EIT, emphasizing the need for tailored approaches that can adapt to the unique challenges of EIT data [17]. Despite this, there remains a notable absence of research specifically targeting the use of MLP in conjunction with semi-supervised learning for cardiac imaging. This gap is critical, as MLPs have shown promise in other imaging modalities for their ability to model complex relationships in data, while semi-supervised learning could leverage unlabeled data to enhance model training and performance [18].

In many studies on image reconstruction for electrical impedance tomography (EIT), the network architecture used often relies on existing models, such as U-Net or previously developed CNN variants. Although these approaches can provide good results, the use of models tailored to the characteristics of EIT data is still limited. In this study, we develop a network architecture from scratch that is optimized for EIT imaging, taking into account the non-linearity and data limitations of electrical impedance reconstruction. This approach allows greater flexibility in tailoring the network to the specific characteristics of the EIT problem.

In light of these considerations, the proposed method aims to develop a robust semi-supervised learning framework utilizing multilayer perceptron networks for cardiac imaging with EIT. This approach will focus on improving the reconstruction of cardiac images through the incorporation of both labeled and unlabeled data. By integrating temporal consistency objectives and disentangled representation learning, the proposed method seeks to optimize the use of available data, thereby addressing the limitations of current EIT reconstruction techniques and contributing to more accurate and reliable cardiac imaging solutions.

II. Related Works

In the context of cardiac imaging, particularly with Electrical Impedance Tomography (EIT) utilizing Multilayer Perceptron (MLP) networks, several studies have contributed to the development of image reconstruction techniques. However, a notable research gap exists in the systematic understanding of optimal neural network architectures specifically tailored for EIT applications.

One relevant study conducted by Huuhtanen and Jung explores anomaly location detection using MLPs in EIT. They highlight that while there is growing interest in employing neural networks for EIT, there remains a lack of comprehensive insights into the most effective architectures for this purpose, particularly in addressing the nonlinear ill-posed inverse problems inherent in EIT [19]. This indicates a significant gap in the literature regarding the specific design and optimization of MLPs for improving the accuracy and reliability of cardiac imaging through EIT.

Another relevant study by Grychtol et al. extends the GREIT framework to three-dimensional imaging, which is particularly beneficial for lung imaging [20]. However, while this study enhances the spatial resolution of EIT images, it does not specifically address the challenges associated with cardiac imaging, such as the dynamic nature of cardiac motion and its impact on image quality. The absence of tailored algorithms that account for cardiac motion represents a critical research gap that could be addressed through the application of multilayer perceptron networks.

Furthermore, the work by Liu et al. introduces a structure-aware sparse Bayesian learning approach for EIT image reconstruction, aiming to enhance image resolution and accuracy [15]. Despite its advancements, the study does not sufficiently explore the integration of machine learning techniques, such as multilayer perceptron networks, which could potentially improve the adaptability and performance of EIT in real-time cardiac imaging scenarios. This indicates a need for further research that combines advanced machine learning methodologies with EIT to optimize cardiac imaging processes.

Lastly, the study by Thurk et al. investigates the effects of individualized EIT settings on regional ventilation distribution assessment, comparing it to traditional imaging methods [21]. While this comparative analysis is valuable, it underscores the necessity for comprehensive evaluations that incorporate both cardiac and respiratory signals in EIT imaging. The lack of studies focusing on the simultaneous reconstruction of cardiac and respiratory information using advanced machine learning techniques presents another significant research gap.

While existing studies provide a foundation for EIT image reconstruction, there is a clear need for research

that systematically optimizes reconstruction parameters, addresses the dynamic nature of cardiac imaging, integrates advanced machine learning techniques, and explores the simultaneous reconstruction of cardiac and respiratory signals. These gaps present opportunities for further investigation in the field of cardiac imaging using EIT and multilayer perceptron networks.

III. Multilayer Perceptron Network Design Architecture

Electrical Impedance Tomography (EIT) is a non-invasive imaging technique that utilizes electrical measurements to reconstruct images of the internal structures of the body, particularly useful in cardiac imaging due to its ability to provide real-time data without the risks associated with ionizing radiation [1]. The proposed method integrates EIT with a Multilayer Perceptron (MLP) network to enhance the accuracy and efficiency of cardiac imaging. Schematic figure EIT for cardiac imaging is depicted in Figure 1.

The proposed system consists of an EIT setup with an array of 16 electrodes placed on the thoracic surface to measure impedance variations caused by cardiac activity. The electrodes will inject low-frequency alternating currents and record the resulting voltage changes, which are indicative of the internal impedance distribution. The collected data will be processed using algorithms Supervised and Semi-Supervised Learning (SSL) to reconstruct the impedance images, which will then be fed into the MLP network for further analysis.

In the data generation and preprocessing phase, a synthetic dataset is created to simulate the impedance distribution of a human thoracic cross-section during cardiac activity. This involves using computational phantoms and solving the forward problem of EIT to calculate voltage measurements at electrode pairs. The forward problem is typically addressed using finite element modeling, which allows for the simulation of voltage distributions under various conditions, including the introduction of noise to mimic real-world scenarios. The dataset is then labeled for supervised learning and partially labeled for semi-supervised learning, ensuring a robust training process for the machine learning models [22].

The dataset is subsequently split into training, validation, and test sets, ensuring a balanced representation of various physiological conditions. For semi-supervised learning, only a subset of the training data is labeled, while the rest remains unlabeled, which is crucial for enhancing model performance in scenarios where labeled data is scarce. The Multilayer Perceptron (MLP) network serves as the primary machine learning model for reconstructing EIT images, consisting of fully connected layers optimized for mapping electrode voltage data to conductivity images. The architecture typically includes three fully connected layers with ReLU, Sigmoid, SoftMax, and tanh activation functions, and the output consists of pixel-wise conductivity values forming a reconstructed image.

Training and evaluation of the model involve both labeled and unlabeled data. In supervised learning, fully labeled data is utilized to train the model using standard backpropagation algorithms, while semi-supervised learning techniques such as pseudo-labeling or consistency regularization are employed to leverage the unlabeled data. Performance metrics such as Mean Squared Error (MSE), Mean Absolute Error (MAE) for reconstruction accuracy and Image Error for image quality assessment are used to evaluate the model's effectiveness, with testing conducted on a separate dataset to assess generalization capabilities.

Multilayer perceptrons (MLP) with at least one hidden layer and a linear output layer are recognized as universal function approximators [23]. Therefore, we approach the function approximation problem by directly training an MLP using simulated training data. To achieve this, we experiment with MLPs by varying the number of hidden layers and the number of neurons in each layer to determine the optimal regression architecture. The resulting architecture is shown in Figure 2, while the hyperparameters used in our experiments are detailed in Table 1.

In an MLP architecture (Figure 2), x is the input to the network that represents the initial data to be processed. Each input is multiplied by a weight w that connects it to a neuron in the next layer. The product of the weights by the input, plus a bias b, produces a linear value z, which is then used as the input to an activation function. The activation applied to z is referred to as a, which serves to add non-linearity to the network so that

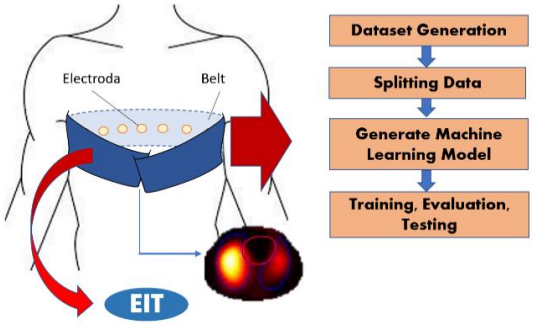

Figure 1. Schematic figure EIT for cardiac imaging

TABLE 1
KEY HYPERPARAMETERS MLP FOR SUPERVISED LEARNING AND SEMI-SUPERVISED LEARNING

Key hyperparameters	Supervised Learning	Semi-supervised Learning
Input layer width	208	208
Hidden layer 1 width	128	256
Hidden layer 2 width	64	128
Hidden layer 3 width	-	64
Hidden layer activation	ReLU, Sigmoid, Softmax, tanh	ReLU, Sigmoid, Softmax, tanh
Output layer width	1912	1912
Output type	Linear	Linear
Optimizer	AdamW	AdamW
Loss function	MSE	MSE
Epochs	100	Initial training: 50 Pseudo-labelling loop: 10/ iteration Total pseudo-labelling iteration: 5 iterations

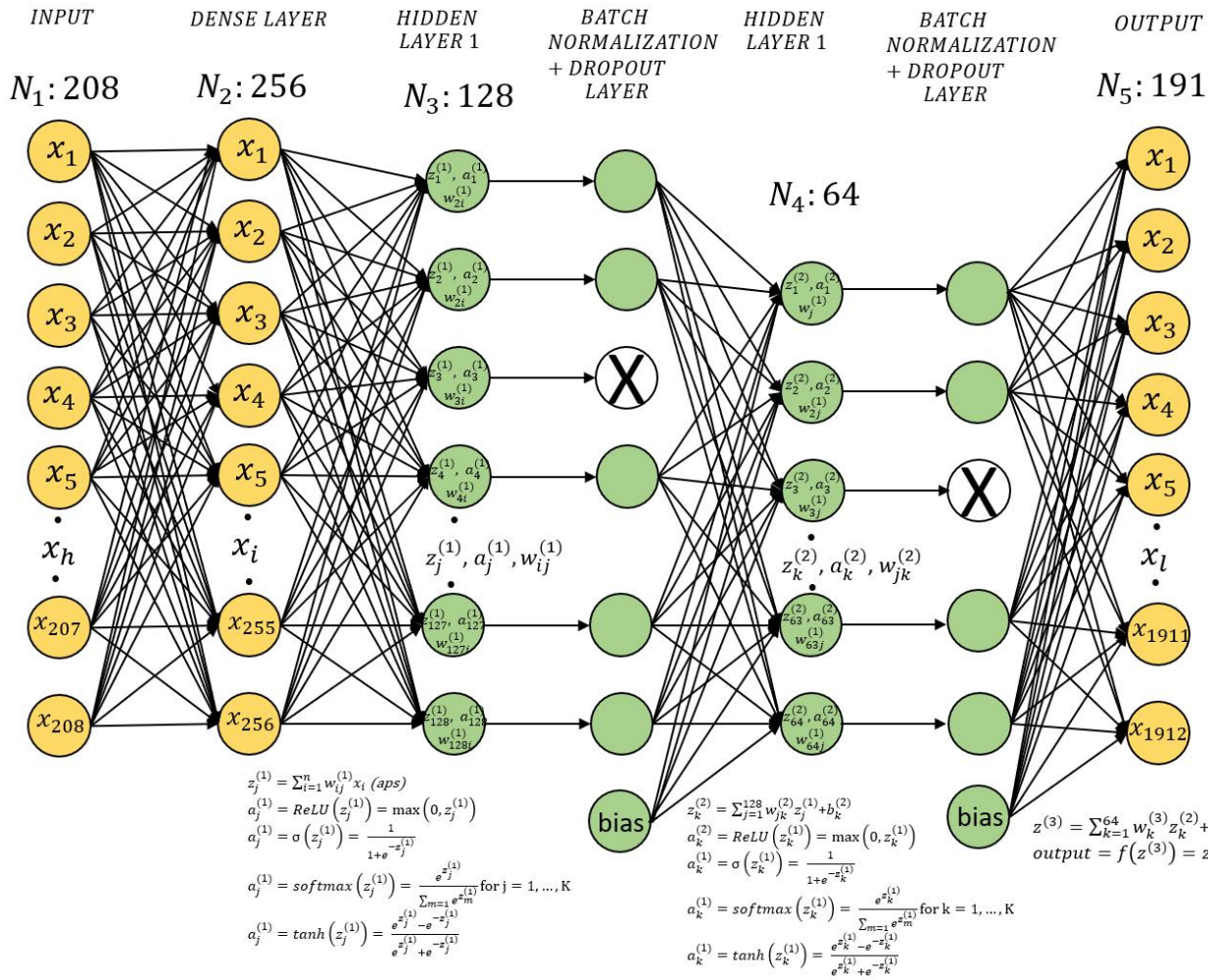

Figure 2. MLP architecture used for Supervised Learning

the model can learn complex relationships in the data. By applying various activation functions such as ReLU, Sigmoid, Softmax, or Tanh.

Supervised learning algorithms need substantial data to achieve strong predictive accuracy. However, in real-world settings like medical diagnosis, image and speech recognition, or document classification, much of the data is unlabeled, which restricts model training on this untagged data. Semi-Supervised Learning provides a solution to this issue by blending Supervised and Unsupervised Learning approaches. Semi-supervised learning is a machine learning method that uses a limited set of labeled data alongside a large set of unlabeled data in the training process [12], [24]. The outcome of Semi-Supervised Learning includes target variables that help train the model and predict outcomes for previously unlabeled data. Experiment with MLPs for Semi-supervised learning by varying the number of hidden layers and the number of neurons in each layer to determine the optimal regression architecture. The hyperparameters used in our experiments are detailed in Table 1.

IV. Experimental Setup and Condition

In this system, we used a phantom that models the thorax with specific shapes and properties to simulate lungs and a heart as depicted in Figure 3. The phantom is designed to reflect realistic biological behaviors such as respiration and cardiac motion.

The thorax phantom is constructed using a mesh-based representation. This thorax has 16 electrodes placed evenly around its perimeter, mimicking the typical setup for EIT measurements. It includes two dynamic lung anomalies and a heart anomaly to replicate physiological conditions:

a. Lungs: Simulated as anomalies with a permittivity of 10.0. The lung radius varies

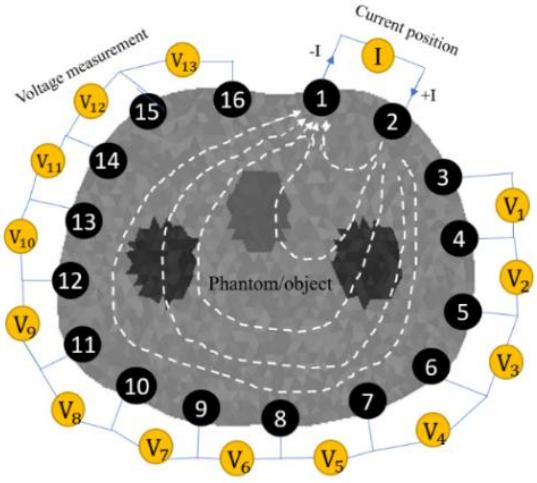

Figure 3. Adjacent Current driven patterns for data acquisition of EIT

cyclically to model the inhale and exhale phases of breathing. Noise is added to introduce slight random fluctuations to the lung size, reflecting natural biological variability.

b. Heart: Positioned slightly below the center of the thorax and modeled as a circular anomaly with a base radius of 0.15 and a small variation (±0.02) to simulate cardiac motion. The permittivity of the heart is set to 5.0, which differs from both lungs and the surrounding thorax tissue.

Thorax synthesis data consists of simulated lung and heart organ data, each of which is distinguished by its permittivity value. Permittivity describes how a material (in this case, biological tissue) responds to an electric field, which is relevant in the physical model of the thorax. EIT image reconstruction simulations are displayed based on differences in conductivity values. In the EIT model, the initial physical simulation using permittivity properties to describe the tissue, but in the reconstruction stage, what is input into the algorithm is a parameter directly measured by EIT, namely electrical conductivity.

As shown in the thorax phantom, these anomalies are updated in every iteration. Lung sizes gradually increase during the inhale phase and decrease during the exhale phase, while the heart anomaly pulsates slightly to simulate its motion. Noise is added to the mesh and voltage measurements to mimic real-world measurement conditions.

For data collection, we applied a neighboring method protocol, where the current is applied between pairs of adjacent electrodes, and the resulting voltages are measured across all other electrode pairs. This method enables a dense dataset of voltage differences, ensuring sufficient information for image reconstruction.

V. Results and Discussion

We conducted algorithm comparisons through simulations using the pyEIT [25] and Keras [26] libraries with synthetic test data. The chosen inverse mesh defined the resolution for modeling lung and heart anomalies to mimic physiological conditions. The lung anomaly diameter was randomly varied within the range d ϵ [0.1, 0.4], while the heart anomaly with a base radius of 0.15, was simulated with a radius variation of 0.02. This set of conductivity values was processed through the pyEIT simulation model to solve the EIT forward problem and generate a frame of voltage measurements, v. To evaluate the performance of different MLP algorithms, we trained MLP-based image reconstruction models using various hyperparameter configurations and activation functions, selecting those that yielded the lowest validation loss (MSE).

We compared regularization techniques by first training the MLP with noise-free training data. We repeated this with all combinations of hyperparameter values and regularization techniques mentioned in Table 1 for supervised and semi-supervised learning. Figures 4–9 show the actual and predicted conductivity distributions for the inhale and exhale conditions. This comparison of distributions involves two learning approaches: supervised learning and semi-supervised learning.

In the inhale condition, the true conductivity distribution (Figure 4) shows a conductivity distribution pattern with two high conductivity areas corresponding to the lung positions. The prediction using supervised learning (Figure 5) produces a distribution that closely resembles the original data, but with a slightly lower spread around the lung area. The prediction using semi-supervised learning (Figure 6) also gives a distribution pattern similar to the actual data, but appears to have better accuracy at the edges than supervised learning.

In the exhale condition, the true conductivity distribution (Figure 7) shows a distribution pattern with a decrease in conductivity in the lung area. The

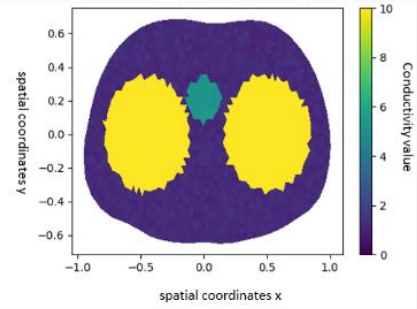

Figure 4. True conductivity distribution while inhale

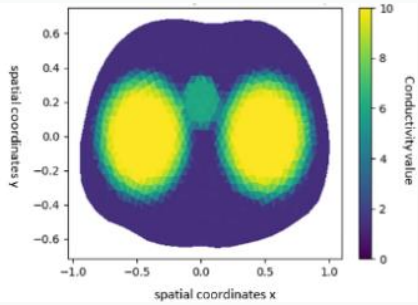

Figure 5. Predicted conductivity distribution while inhale for Supervised Learning

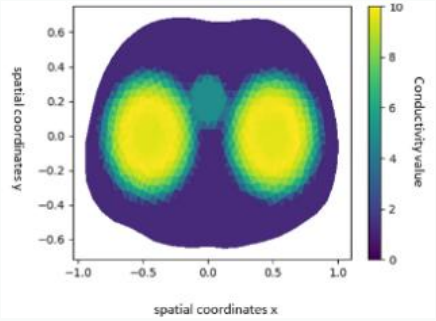

Figure 6. Predicted conductivity distribution while inhale for Semi-supervised Learning

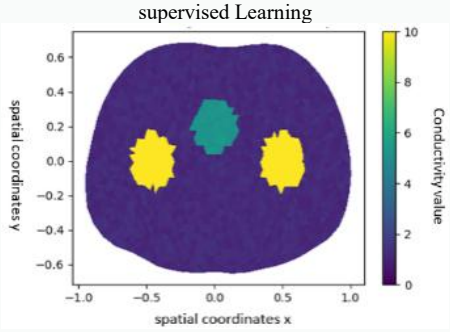

Figure 7. True conductivity distribution while exhale

prediction using supervised learning (Figure 8) is close to the actual data, but the distribution is flatter around the lung core. Semi-supervised learning (Figure 9) provides results that are more in line with the actual pattern, especially in the more focused lung core distribution area. From visual analysis, semi-supervised learning shows a better ability to capture complex distribution patterns, especially in areas with sharp gradients.

The reconstructed images of the conductivity distribution during inhalation and exhalation (Figures 5–9) show that the semi-supervised learning method provides smoother results and is closer to the actual conductivity distribution compared to the supervised learning method. The main difference is seen in the boundary area between two regions with different conductivity values, where semi-supervised learning shows a reduction in noise and artifacts.

Table 2 provides quantitative results based on MSE values for various combinations of activation functions and dropouts in supervised and semi-supervised learning approaches. In general, supervised learning has a lower MSE than semi-supervised learning. This is expected because the semi-supervised approach uses less labeled data, so the prediction accuracy decreases. However, the performance degradation of semi-supervised learning is still within acceptable limits, with an average MSE difference of around 0.1–0.3.

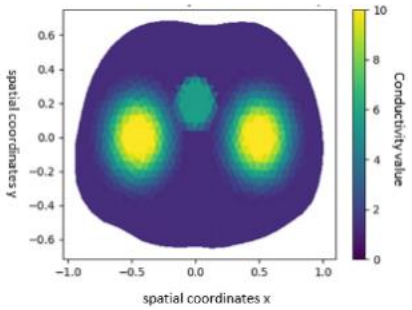

Figure 8. Predicted conductivity distribution while exhale for Supervised Learning

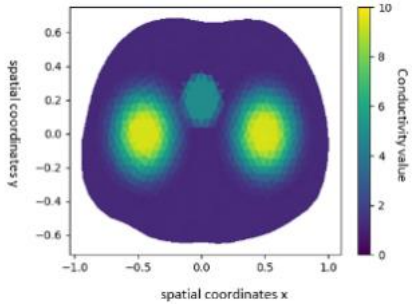

Figure 9. Predicted conductivity distribution while exhale for Semi-supervised Learning

TABLE 2
COMPARISON OF MSE FOR REGULARIZATION TECHNIQUE

Activation	Dropout	MSE	
		Supervised Learning	Semi-supervised Learning
ReLU	**0.1**	5.18	5.57
	0.3	5.04	5.40
	0.5	5.01	5.19
Sigmoid	**0.1**	4.86	5.17
	0.3	4.79	5.13
	0.5	4.76	5.08
Softmax	**0.1**	4.94	5.49
	0.3	4.90	5.22
	0.5	4.86	5.12
tanh	**0.1**	5.01	5.29
	0.3	4.94	5.28
	0.5	4.90	5.24

Supervised learning has a lower MSE than semi-supervised learning indicating that the model with supervised learning is more accurate in predicting the conductivity distribution. A higher dropout rate (0.5) gives the best results for most activation functions, especially for Sigmoid and ReLU (lowest MSE: 4.76 for Sigmoid with dropout 0.5). Although semi-supervised learning produces a slightly higher MSE, this result indicates the potential for using less data than supervised learning. A dropout rate of 0.3 provides a good balance for both ReLU and Sigmoid activation functions.

Dropout stability in Semi-supervised Learning is obtained when the dropout value is 0.3, which is the middle value that provides an optimal balance between preventing overfitting and maintaining the model's representation capacity. The result is a relatively lower and consistent MSE across most activation functions. Meanwhile, too low a dropout (0.1) in semi-supervised learning tends to result in overfitting, because the model is less able to handle noise in the training data, especially when some of the data is unlabeled. Conversely, if the dropout is too high (0.5) it tends to cause underfitting, where the model loses important information because too many neurons are deactivated during training.

The ReLU activation function shows stable performance with competitive MSE in both supervised and semi-supervised methods. Notably, the Sigmoid function achieved the lowest MSE of 4.76 in supervised learning when combined with a dropout rate of 0.5, indicating that this configuration enables the model to learn more effectively and generalize well to the target output. In contrast, both Softmax and tanh functions produce slightly higher MSE than ReLU and Sigmoid, but remain competitive, especially at a dropout of 0.3 for semi-supervised learning.

The impact of adding a dropout of 0.3 provides the best balance between generalization and accuracy for most activation functions. In contrast,. a dropout rate of 0.1 resulted in higher MSE values, suggesting insufficient regularization capacity. Dropout 0.5 shows a decrease in MSE in supervised learning, but slightly increases MSE in semi-supervised learning.

The semi-supervised learning approach has good potential to be applied to limited labeled data such as electrical impedance tomography. Although the MSE of this approach is higher than supervised learning, the visual results show that this approach is able to reconstruct the conductivity distribution pattern well.

Figure 10 illustrates the smooth and periodic nature of the lung's inhale-exhale cycle, with lung size increasing during inhalation and decreasing during exhalation. The cycle follows a sinusoidal pattern, indicating that the data represents the dynamic changes in lung volume accurately. This smooth and symmetric pattern provides a strong foundation for analyzing the

image prediction error across the inhale-exhale phases using supervised and semi-supervised learning methods. This graph (Figure 10) only shows the breathing pattern (expanding and deflating). However, in the mesh-based simulation, no changes in the shape of the lung are actually made. Only the electrical conductivity values are changed, not the mesh shape. So, the mesh remains stationary, only the data mathematically describe the changes in breathing.

In this simulation, lung size is modeled as a sinusoidal function that oscillates between a minimum value of 0.1 (exhalation) and a maximum value of 0.4 (inhalation). These results indicate that during the breathing process, the lung size changes by about 75% of its maximum size when moving from exhalation to inhalation. This value is still within the range of reasonable lung volume changes according to physiological studies [25].

Figure 11 shows the image error (IE) across the continuous inhale-exhale cycle for supervised learning. During the inhalation phase (0-6 seconds), the error gradually increases, peaking around 2-3 seconds before decreasing as the cycle approaches the transition to exhalation. This increase is likely due to the challenges of capturing rapid changes in conductivity distribution during the early stages of lung expansion. During the exhalation phase (6-12 seconds), the error decreases initially but slightly increases again toward the end of the cycle, potentially due to the model's limitations in capturing minor variations in conductivity at the end of exhalation. Overall, supervised learning demonstrates relatively low and stable error values throughout the cycle, indicating its effectiveness in predicting the distribution of conductivity accurately.

Figure 12 presents the image error over the inhale-exhale cycle for semi-supervised learning. Similar to supervised learning, the error increases during the early inhalation phase and peaks around 2-3 seconds. However, the overall error values are slightly higher than those observed in supervised learning. During exhalation, the error decreases but exhibits more noticeable fluctuations compared to supervised learning, particularly toward the end of the cycle. This indicates that while semi-supervised learning can capture the general trend of the cycle, it struggles with finer details and exhibits less stability, likely due to the limited availability of labeled data during training.

When comparing the two methods, supervised learning outperforms semi-supervised learning in terms of accuracy and stability, with lower error values and smaller fluctuations throughout the cycle. The results highlight the advantage of using fully labeled data for accurately modeling complex changes in conductivity during the inhale-exhale cycle. However, semi-supervised learning still shows promise by providing reasonable predictions with less reliance on labeled data, making it a practical alternative when fully labeled datasets are unavailable

VI. Conclusion

The main contribution of this research is the development of a network architecture specifically

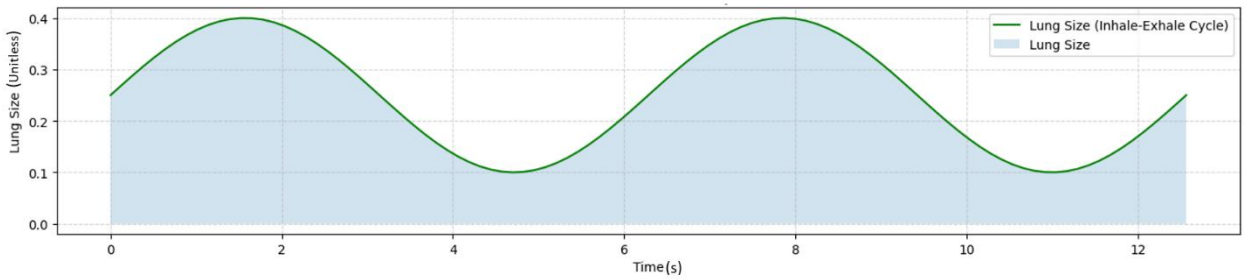

Figure 10. Smooth inhale-exhale cycle of lung cardiac

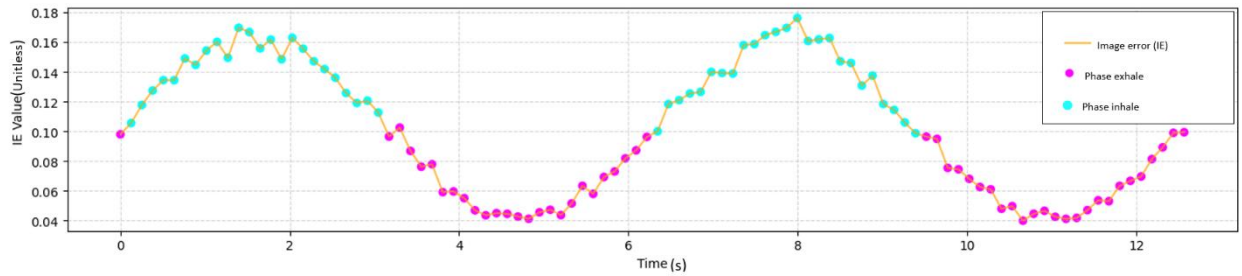

Figure 11. Image error over continuous inhale-exhale cycle for Supervised learning

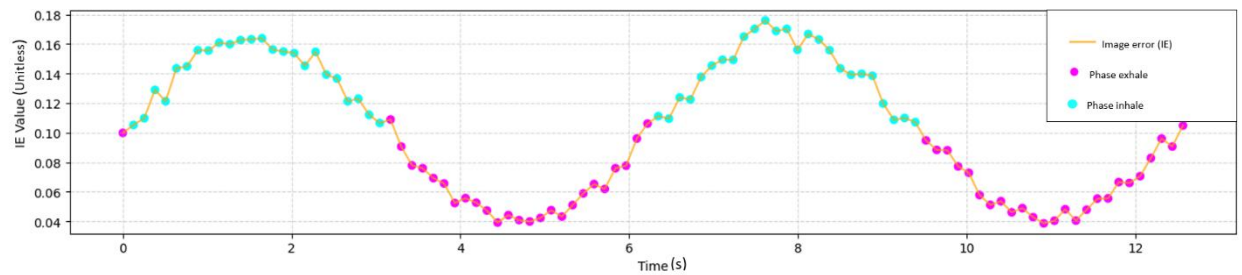

Figure 12. Image error over continuous inhale-exhale cycle for Semi-supervised learning

designed for EIT imaging, which has been shown to improve reconstruction accuracy compared to previous approaches. The semi-supervised learning approach shows great potential for image reconstruction in electrical impedance tomography, especially when labeled data are limited. Despite having slightly higher MSE values than supervised learning, this method is able to reconstruct the conductivity distribution well, especially in areas with complex gradients such as inhale and exhale conditions. The Sigmoid and Tanh activation functions and the use of a dropout of 0.3 provide the most stable and accurate results in both approaches.

These results confirm that semi-supervised learning can be an efficient and effective alternative in tomography applications. By reducing the dependence on fully labeled data, this method allows for cost and time savings in data collection. For further development, optimization of model parameters and integration with data enhancement techniques can improve the accuracy and generalization of this approach.

In terms of image error (IE), supervised learning method shows better performance with lower and stable error throughout the inhalation-exhalation cycle, indicating the ability of the model to predict the conductivity distribution with high accuracy. In contrast, the semi-supervised learning method yields higher errors and greater fluctuations, especially during the transition between inhalation and exhalation phases. This suggests limitations in capturing dynamic conductivity changes with the same level of precision, due to the reduced availability of labeled data. Nevertheless, semi-supervised learning still demonstrates reasonably accurate predictions, with lower accuracy compared to supervised method. Data collection is preferably done in the exhalation phase, because in this phase the model shows better performance with lower and more consistent error. The transition between inhalation and exhalation can be a more difficult point to predict, so avoiding the transition phase and focusing on exhalation can provide more optimal results in terms of prediction accuracy.

DECLARATIONS

CONFLICT OF INTEREST

The authors have declared that no competing interests exist.

CREDIT AUTHORSHIP CONTRIBUTION

A.P. Ristyawardani: Writing-Reviewing, Editing, Investigation, Software; M.R. Baidillah: Conceptualization, Writing-Original draft preparation, Writing-Reviewing, Editing, Visualization, Investigation, Software, Funding Acquisition; Y. Adityawarman: Supervision, Hardware; P. Busono: Supervision, Funding Acquisition; M.A. Rachmadi: Hardware; M. Yantidewi: Supervision; E. Rahmawati: Supervision

Funding

This paper was funded by Riset dan Inovasi untuk Indonesia Maju (RIIM) Kompetisi (Batch: RIIM 2024-02 (G6) Kode: RIIM-572542113949, SK No. 40/II.7/HK/2024), fiscal year 2024 with title of project: PENCITRAAN JANTUNG BERBASIS TOMOGRAFI IMPEDANSI LISTRIK.

Acknowledgment

We thank our colleagues from the Bioelectronics and Biosensing Laboratory, Research Center for Electronics BRIN, who provided insight and expertise that greatly assisted this research.

REFERENCES

[1] H. V. Tran, M. H. Kim, T. C. Le, and Y. Yoon, "High accurate and efficient electrical impedance tomography for fast brain imaging," 2023, doi: 10.1117/12.2659172.

[2] A. Z. Hayat, A. T. Nugroho, and N. Priyantari, "Prototype portable electrical resistance tomography," *IPTEK J. Technol. Sci.*, vol. 32, no. 3, p. 136, 2022, doi: 10.12962/j20882033.v32i3.8843.

[3] G. Y. Jang *et al.*, "Noninvasive, simultaneous, and continuous measurements of stroke volume and tidal volume using eit: feasibility study of animal experiments," *Sci. Rep.*, vol. 10, no. 1, pp. 1–12, 2020, doi: 10.1038/s41598-020-68139-3.

[4] D. A. Nguyen, P. Qian, M. Barry, and A. McEwan, "Self- weighted noser- prior electrical impedance tomography using internal electrodes in cardiac radiofrequency ablation," *Physiol. Meas.*, vol. 40, p. 065006, 2019, doi:10.1088/1361- 6579/ab1937.

[5] C. Putensen, B. Hentze, S. Muenster, and T. Muders, "Electrical impedance tomography for cardio-pulmonary monitoring," *J. Clin. Med.*, vol. 8, no. 8, 2019, doi: 10.3390/jcm8081176.

[6] A. Santini, E. Spinelli, T. Langer, S. Spadaro, G. Grasselli, and T. Mauri, "Thoracic electrical impedance tomography: an adaptive monitor for dynamic organs," *J. Emerg. Crit. Care Med.*, vol. 2, no. September, pp. 71–71, 2018, doi: 10.21037/jeccm.2018.08.08.

[7] J. Caruana, J. Paratz, A. Chang, A. Barnett, and J. Fraser, "The time taken for the regional distribution of ventilation to stabilise: an investigation using electrical impedance tomography," *Anaesth. Intensive Care*, vol. 43, pp. 88–91, 2015, doi:10.1177/0310057X1504300113.

[8] S. Kumar and R. Kumar, "Analysis and validation of medical application through electrical impedance based system," *International Journal of Intelligent Systems and Applications in Engineering*, vol. 1, no. 6. pp. 14–18, 2018. doi: 10.18201/ijisae.2018637925.

[9] S. J. Hamilton and A. Hauptmann, "Deep d-bar: real-time electrical impedance tomography imaging with deep neural networks," *IEEE Trans. Med. Imaging*, vol. 37, no. 10, pp. 2367–2377, 2018, doi: 10.1109/TMI.2018.2828303.

[10] F. Song, X. Xu, and Y. Dong, "A spatially adaptive total variation regularization method for electrical resistance tomography," *Meas. Sci. Technol.*, vol. 26, no. 12, p. 125401, 2015, doi:10.1088/0957- 0233/26/12/125401.

[11] L. Karrach and E. Pivarčiová, "Using different types of artificial neural networks to classify 2d matrix codes and their rotations—a comparative study," *J. Imaging*, vol. 9, no. 9, pp. 1–16, 2023, doi: 10.3390/jimaging9090188.

[12] J. E. van Engelen and H. H. Hoos, "A survey on semi-supervised learning," *Mach. Learn.*, vol. 109, no. 2, pp. 373–440, 2020, doi: 10.1007/s10994-019-05855-6.

[13] C. S. Perone and J. Cohen-Adad, "Deep semi-supervised segmentation with weight-averaged consistency targets," *Lect. Notes Comput. Sci. (including Subser. Lect. Notes Artif. Intell. Lect. Notes Bioinformatics)*, vol. 11045 LNCS, pp. 12–19, 2018, doi: 10.1007/978-3-030-00889-5_2.

[14] E. Endarko and A. B. Sanjaya Umbu, "Design of low-cost and simple reconstruction method for three dimensional electrical impedance tomography (3d-eit) imaging," *J. Penelit. Fis. dan Apl.*, vol. 10, no. 2, p. 125, 2020, doi: 10.26740/jpfa.v10n2.p125-136.

[15] S. Liu, J. Jia, Y. D. Zhang, and Y. Yang, "Image reconstruction in electrical impedance tomography based on structure-aware sparse bayesian learning," *IEEE Trans. Med. Imaging*, vol. 37, no. 9, pp. 2090–2102, 2018, doi: 10.1109/TMI.2018.2816739.

[16] A. Zhang, Ke and Li, Maokun and Liang, Haiqing and Wang,

Juan and Xu, Shenheng and Abubakar, "Deep feature-domain matching for cardiac-related component separation from image series of chest electrical impedance tomography: proof-of-concept study," *Physiol. Meas.*, vol. 43, 2022, doi: 10.1088/1361-6579/ac9c44.

[17] T. Rymarczyk, G. Kłosowski, E. Kozłowski, J. Sikora, and P. Adamkiewicz, "Improving the tomographic image by enhancing the machine learning algorithm," *J. Phys. Conf. Ser.*, vol. 2408, no. 1, 2022, doi: 10.1088/1742-6596/2408/1/012020.

[18] T. Rymarczyk, G. Klosowski, E. Kozlowski, and P. Tchórzewski, "Comparison of selected machine learning algorithms for industrial electrical tomography," *Sensors (Switzerland)*, vol. 19, no. 7, 2019, doi: 10.3390/s19071521.

[19] T. Huuhtanen and A. Jung, "Anomaly location detection with electrical impedance tomography using multilayer perceptrons," *IEEE Int. Work. Mach. Learn. Signal Process. MLSP*, vol. 2020-Septe, 2020, doi: 10.1109/MLSP49062.2020.9231818.

[20] B. Grychtol, B. Müller, and A. Adler, "3D eit image reconstruction with greit," *Physiol. Meas.*, vol. 37, no. 6, pp. 785–800, 2016, doi: 10.1088/0967-3334/37/6/785.

[21] F. Thürk *et al.*, "Effects of individualized electrical impedance tomography and image reconstruction settings upon the assessment of regional ventilation distribution: comparison to 4-dimensional computed tomography in a porcine model," *PLoS One*, vol. 12, no. 8, pp. 1–16, 2017, doi: 10.1371/journal.pone.0182215.

[22] Z. Han and S. Yin, "Research on semi-supervised classification with an ensemble strategy," vol. 136, no. Icsma, pp. 681–684, 2016, doi: 10.2991/icsma-16.2016.119.

[23] K. Hornik, M. Stinchcombe, and H. White, "Multilayer feedforward networks are universal approximators," *Neural Networks*, vol. 2, no. 5, pp. 359–366, 1989, doi: 10.1016/0893-6080(89)90020-8.

[24] T. Miyato, S. I. Maeda, M. Koyama, and S. Ishii, "Virtual adversarial training: a regularization method for supervised and semi-supervised learning," *IEEE Trans. Pattern Anal. Mach. Intell.*, vol. 41, no. 8, pp. 1979–1993, 2019, doi: 10.1109/TPAMI.2018.2858821.

[25] S. W. Basuki, I. Primasakti, and R. Sari, "Perbedaan nilai rerata kvp % prediksi dan kv % prediksi antara orang dengan indeks massa tubuh normal dan di atas normal," *Biomedika*, vol. 8, no. 1, pp. 8–14, 2016, doi: 10.23917/biomedika.v8i1.3022.